Optical model potential analysis of $\overline{n}A$ and nA interactions

Teck-Ghee Lee[1] and Cheuk-Yin Wong[2]

[1]*Department of Physics, Auburn University, Auburn, Alabama 36849, USA*
[2]*Physics Division, Oak Ridge National Laboratory, Oak Ridge, Tennessee 37831, USA*

We use a momentum-dependent optical model potential to analyze the annihilation cross sections of the antineutron $\overline{n}$ on C, Al, Fe, Cu, Ag, Sn, and Pb nuclei for projectile momenta $p_{\mathrm{lab}} \lesssim 500$ MeV/c. We obtain a good description of annihilation cross section data of Barbina *et al.* [Nucl. Phys. A **612**, 346 (1997)] and of Astrua *et al.* [Nucl. Phys. A **697**, 209 (2002)] which exhibit an interesting dependence of the cross sections on p_{lab} as well as on the target mass number A. We also obtain the neutron (n) nonelastic reaction cross sections for the same targets. Comparing the nA reaction cross sections $\sigma_{\mathrm{rec}}^{nA}$ to the $\overline{n}A$ annihilation cross sections $\sigma_{\mathrm{ann}}^{\overline{n}A}$, we find that $\sigma_{\mathrm{ann}}^{\overline{n}A}$ is significantly larger than $\sigma_{\mathrm{rec}}^{nA}$, that is, the $\sigma_{\mathrm{ann}}^{\overline{n}A}/\sigma_{\mathrm{rec}}^{nA}$ cross section ratio lies between the values of about 1.5 to 4.0 in the momentum region where comparison is possible. The dependence of the $\overline{n}$ annihilation cross section on the projectile charge is also examined in comparison with the antiproton $\overline{p}$. Here we predict the $\overline{p}A$ annihilation cross section on the simplest assumption that both $\overline{p}A$ and $\overline{n}A$ interactions have the same nuclear part of the optical potential but differ only in the electrostatic Coulomb interaction. Deviation from a such simple model extrapolation in measurements will provide new information on the difference between $\overline{n}A$ and $\overline{p}A$ potentials.

I. INTRODUCTION

Annihilation between an antinucleon and a nucleon or nucleus defines one of the basic aspects in antimatter-matter interactions. Over the years there have been many experimental measurements [1–21] and theoretical studies [21–41] about antinucleon annihilation on nucleons and nuclei. However, most of the work was carried out with the antiproton $\overline{p}$ projectile. Experimental and theoretical investigations using the antineutron $\overline{n}$, on the other hand, are still relatively limited. Theoretical work has also been carried out on the relationship between $\overline{n}n$ oscillation and the $\overline{n}A$ interaction potential [42–44]. Recently, it has also been suggested that $\overline{n}A$ annihilation can be used to prepare an apparatus for $\overline{n}n$ oscillation [45] detection.

On the experimental side, one representative investigation is the measurement of the $\overline{n}$Fe annihilation cross section from 100 to 780 MeV/c [46–48]. The experiment was carried out with the LEAR facility at CERN using the $\overline{p}p \rightarrow \overline{n}n$ charge-exchange reaction. Another investigation, by the OBELIX group of Astrua *et al* [8], measured the annihilation cross section of $\overline{n}$ on C, Al, Cu, Ag, Sn, and Pb nuclei in the p_{lab} range from 50 to 400 MeV/c. These experiments give clear evidence about the dependence of the antinucleon-nucleus absorption cross section on the mass number A and about the momentum dependence, which exhibits the prominent absorption feature of inverse-power-law type of momentum dependence at low energies. They are also useful to test the theories of antinucleon-nucleus interactions.

In response to the experimental efforts, Friedman derived an optical model potential for $\overline{p}$-nucleus interaction by accounting for both the neutron and proton densities [32] to examine the

annihilation cross sections for $\overline{p}$ and $\overline{n}$ on all the six targets at seven energies studied in Astrua *et al* [8]. The calculated cross sections for $\overline{p}$ and $\overline{n}$ were compared with experimental annihilation cross sections for $\overline{n}$. The study indicated that the $\overline{p}$ induced annihilation cross sections increase much more steeply in the low momentum $p_{\mathrm{lab}} < 200$ MeV/c region in comparison to the case for the $\overline{n}$ projectile. It also elucidated that the larger $\overline{p}$ annihilation cross sections match the experimental data closely, but surprisingly not for $\overline{n}$ annihilation cross sections. Above 250 MeV/c, the $\overline{n}$ annihilation cross sections are found to be reasonably close to the experimental cross sections. However, below 100 MeV/c, the cross sections are found to be significantly smaller than the experimental cross sections. Furthermore, the predicted $\overline{n}$ annihilation cross sections display the feature of decreasing and shifting to lower and lower momenta as the size of the nuclear target increases, and thus deviate from the behavior suggested by the experimental cross sections. It is important to note that the very same density-folded optical model potential was checked and tested previously, by the same author of Ref. [32], to reproduce very well the angular distributions for elastic scattering of $\overline{p}$ by C, Ca, and Pb at 300 MeV/c [31].

The fact that $\overline{n}$ induced annihilation cross sections are smaller than for $\overline{p}$ can be easily understood because the incoming electrically neutral projectile will naturally experience negligible Coulomb attraction from the target nucleus. But, it is perplexing that experimentally there is a notable absorption feature of $1/p_{\mathrm{lab}}^{\alpha}$-like dependence, akin to the effects of Coulomb focusing for $\overline{n}$ annihilation cross sections at lower momenta, and the microscopic optical potential predicted that these cross sections decrease and shift to lower and lower momenta as A increases.

Recently, we extended the Glauber model for nucleus-nucleus collisions [49–52] to study the nuclear annihilation cross sections by antinucleons. The extended Glauber model for the calculation of the $\overline{p}A$ annihilation cross section [22,23] considered the nucleon-nucleus collision as a collection of binary collisions, and took into account the appropriate shadowing and the inclusion of initial-state and in-medium interactions. The basic ingredients are the elementary $\overline{p}p$ and $\overline{p}n$ annihilation cross sections, $\sigma_{\rm ann}^{\overline{p}p}$ and $\sigma_{\rm ann}^{\overline{p}n}$, together with initial-state Coulomb interactions and the change of the momentum of the antinucleon inside the nuclear medium. We note that, in our earlier study [22], the basic $\overline{p}p$ annihilation cross section, $\sigma_{\rm ann}^{\overline{p}p}$, was parametrized semi-empirically as $1/v$ and employed in our investigation of the stability and the properties of matter-antimatter molecules [53,54]. In our subsequent study [23], we improved the $\sigma_{\rm ann}^{\overline{p}p}$ and $\sigma_{\rm ann}^{\overline{p}n}$ formulas by considering the antiparticle transmission through a nuclear potential and the $\overline{p}p$ Coulomb interaction, thereby the nuclear annihilation cross sections can be properly evaluated in a simple analytical form. The expressions are rigorous enough and therefore we amend our earlier simple approach of a $1/v$ function to parametrize the basic $\sigma_{\rm ann}^{\overline{p}p}$ and $\sigma_{\rm ann}^{\overline{p}n}$ cross sections. The strong absorption model formulated decomposes the incoming plane waves into a sum of partial waves of given orbital angular momentum L and assumes that these partial waves transmitted to the nucleon surface S lead to an annihilation reaction. It is shown that the cross sections for nuclear annihilation by $\overline{p}$ and $\overline{n}$ are simple functions of the momentum of the incident particles. Across the momentum range considered, contrasting it to the $\sigma_{\rm ann}^{\overline{n}p}$ annihilation cross section, the $\sigma_{\rm ann}^{\overline{p}p}$ annihilation cross section is significantly enhanced by the Coulomb interaction for $p_{\rm lab}$ momenta of the incident particle below 500 MeV/c. As $p_{\rm lab}$ increases, the two annihilation cross sections become almost identical, approaching Pomeranchuk's equality limit [55] at $p_{\rm lab} \sim 500$ MeV/c. In addition, the calculated annihilation cross sections agree well with the experimental data. With the improved $\sigma_{\rm ann}^{\overline{p}p}$ and $\sigma_{\rm ann}^{\overline{p}n}$, we also reproduced the general map of annihilation cross sections, $\sigma_{\rm ann}^{\overline{p}A}$, as a function of nuclear mass numbers A and collision energies.

With encouraging results from the particle transmission theory to describe the $\sigma_{\rm ann}^{\overline{p}p}$, $\sigma_{\rm ann}^{\overline{p}n}$, and $\sigma_{\rm ann}^{\overline{p}A}$ annihilation cross sections, we employed the very same theory to examine $\sigma_{\rm ann}^{\overline{n}A}$. But there was an inadvertent error that arose through the Coulomb trajectory modification considered in the extended Glauber model, making our $\sigma_{\rm ann}^{\overline{n}A}$ agree with the experiment data. We reexamined and reevaluated our $\sigma_{\rm ann}^{\overline{n}A}$ cross section and found, in the absence of additional Coulomb effects, that the rectified $\sigma_{\rm ann}^{\overline{n}A}$ cross sections are significantly "flat" and relatively lower than the experimental data for $p_{\rm lab} < 200$ MeV/c, yielding a far from satisfactory agreement between our calculations and experiment of Astrua *et al.*

Anticipating that new and better experiments [56–58] will be performed in the coming years, here we attempt to explore an alternative theoretical method to rectify our previous annihilation cross section results for $\overline{n}A$. Moreover, it appears that a comparative study of the absorption cross sections induced by neutrons, antineutrons, and antiprotons has not yet been made.

The content of this paper is as follows. In Sec. II, we present the phenomenological optical model potential (OMP) we obtained to examine the $\overline{n}A$ annihilation cross sections. In Sec. III, we assess our phenomenological theory by comparing our numerical results to the available experimental $\overline{n}A$ annihilation cross section, nA reaction cross section, and $\overline{p}A$ annihilation data. Finally, we conclude the present study with some discussions in Sec. IV.

II. PHENOMENOLOGICAL MOMENTUM-DEPENDENT OPTICAL MODEL POTENTIAL

The Glauber model is known to work best at high energies in which the extend individual nucleon can be treated as an isolated scatterer. For low-energy collisions, such a description may not be appropriate, and the traditional optical model potential analysis may be more suitable. For this reason we adopt a phenomenological analysis to study the energy dependence of the OMP on $\overline{n}A$ annihilation cross section. Moreover, the method of OMP is well tested and long established for treating complicated interactions between an incoming nucleon and a nucleus [59,60].

In the present analysis, we consider the collision between an antinucleon (an $\overline{n}$ or an $\overline{p}$ and, or a neutron) and a nucleus, and their effective interaction strength without spin-orbit interaction is represented generally by a momentum-dependent optical model potential,

$$U(r) = V_C(r) - V_V(r,p) - i[W_V(r,p) + W_D(r,p)], \quad (1)$$

where subscripts V and D denote the volume and surface terms, respectively; and

$$V_V(r,p) = V_o(p)f(r,r_V,a_V), \quad (2)$$

$$W_V(r,p) = W_o(p)f(r,r_W,a_W), \quad (3)$$

$$W_D(r,p) = -4a_{W_D}W_{o_D}(p)\frac{d}{dr}f(r,r_{W_D},a_{W_D}). \quad (4)$$

As usual the $f(r,r_x,a_x)$ is a Wood-Saxon form factor,

$$f(r,r_x,a_x) = \frac{1}{(1 + \exp[(r - r_x)/a_x])}, \quad (5)$$

where $x \equiv V, W, W_D$. The Coulomb term $V_C(r)$ is naturally zero for an electrically neutral projectile. Otherwise,

$$V_C(r) = \begin{cases} \frac{Z_A Z_p e^2}{2r_c}\left(3 - \frac{r^2}{r_c^2}\right) & \text{for } r \leqslant r_c, \\ \frac{Z_A Z_p e^2}{r} & \text{for } r > r_c, \end{cases} \quad (6)$$

for a charged projectile, with Z_A and Z_p being the target and projectile nuclear charges, respectively, and $r_c = r_o A^{1/3}$ is the Coulomb radius with r_o being 1.25 fm.

Although the main focus here is the $\overline{n}A$ optical model potential, our knowledge of the $\overline{p}A$ optical model potential is more extensive. To gain some intuitions about the shape and size of our desired OMP, knowledge of the $\overline{p}A$ OMP is valuable as it could shed some light on the construction of $\overline{n}A$ OMP. There are at least two families of the $\overline{p}A$ potential, and these families and their ambiguity were studied by one of the present authors in [61]. One family, so-called S, has

a much more shallow imaginary potential with W of order 15–45 MeV, associated with a deep real potential with V of order 200–350 MeV. The other one, so-called D, has a real well depth V of order 100 MeV and a deep imaginary part W of order 100–200 MeV. On the other hand, the neutron-nucleus (nA) optical potential is also well established. From Koning and Delaroche [60], we learned that the nA optical potential has a real well depth V of the order of 60 MeV and considerably shallower imaginary potential with W of the order of 15 MeV for many nuclei across the periodic table, but with A value greater than 23. This potential family is quite different from that of $\bar{p}A$.

The optical model potential of Koning and Delaroche has many advantages because of its simplicities and systematic variations. However, as it has not taken into account the effects of static and dynamical deformation of the nuclei, it has its limitations, and its application to ^{12}C as we do here will exhibit an expected deficiency.

It is desirable to have a simple, "flexible," and yet rich enough (i.e., applicable in the very-low-momentum region) form of optical model potential for $\bar{n}A$ that could also be useful for $\bar{p}A$ annihilation. We therefore concocted a momentum-dependent phenomenological optical model potential,

$$V_o(p_{\text{lab}}) = V_o' \times \left(\frac{\cosh(\sqrt{(b_0 + p_{\text{lab}})} - \sqrt{b_0})}{\cosh(\sqrt{(b_1 + p_{\text{lab}})} - \sqrt{b_1})} \right), \quad (7)$$

where b_0 and b_1 are two adjustable parameters. We choose this form so that $V_o \to V_o'$ as $p_{\text{lab}} \to 0$, and we use the cosh function such that $V_o(p_{\text{lab}})$ decreases monotonically and gradually with p_{lab}. In addition, we also want our $V_o(p_{\text{lab}})$ to behave similarly to the functional dependence of $V_V(E)$ of Koning and Delaroche plotted in Fig. 1 of Ref. [60]. We
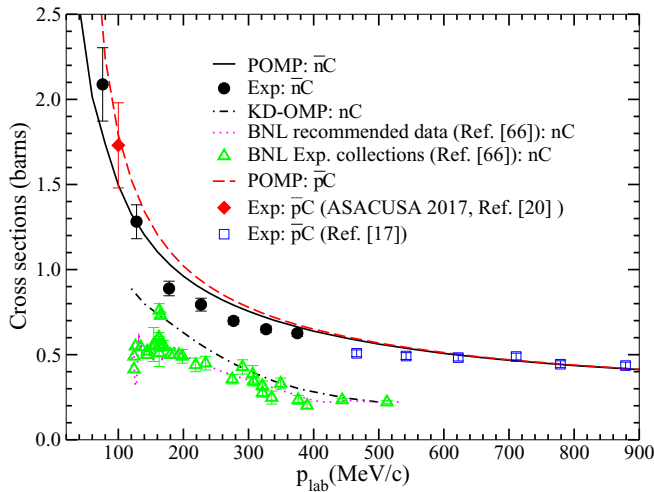

FIG. 1. Comparison of $\bar{n}$C, $\bar{p}$C annihilation cross sections and the nC nonelastic reaction cross section as a function of the projectile momentum in the laboratory frame. The dash-dot-dotted line refers to the nC reaction cross section obtained using the KD-OMP; the dotted line and the scattered triangles are the nC reaction nonelastic data from Brookhaven National Laboratory's National Nuclear Data Center [66].

TABLE I. Antineutron optical model potential well depths, V_o' and $W_{(o,oD)}$, and the $b_{(0,1)}$ free parameters, are in MeV, and $V_D = 0$. The $W_{(o,oD)}$ parameters are independent of the projectile momentum.

Nucleus	^{12}C	^{27}Al	^{56}Fe	$^{63.6}$Cu	$^{107.9}$Ag	$^{118.7}$Sn	^{206}Pb
V_o'	52.00	66.00	56.00	60.00	82.00	90.00	110.00
W_o	12.00	3.50	9.00	4.33	4.10	4.30	2.80
W_{oD}	5.98	5.98	5.98	5.98	5.98	5.98	5.98
b_0	14.04	31.86	67.20	75.52	127.29	140.08	243.08
b_1	7.92	16.90	39.00	37.70	61.10	65.00	106.60

also assume that our absorptive potentials, $W_o(p) = W_o$ and $W_{oD}(p) = W_{oD}$, do not vary with the projectile momentum. Table I lists the optical model potential well depths and the b_0 and b_1 parameters used in the calculations.

With regard to the radius parameter in the optical potential, we use the following procedure to estimate its approximate value before more refined search and adjustment. From the experimental annihilation cross section at high energies at which a geometrical approximation is a reasonable assumption, we estimate a radius r_R given by

$$\sigma_{\text{ann}} = \pi (r_R A^{1/3})^2. \quad (8)$$

This radius defines a sharp cutoff distribution for the collision process. The equivalent Wood-Saxon optical model potential with a radius parameter of r_V and a diffuseness a_V can be estimated by [62]

$$r_V = r_R \left(1 - \frac{1}{3} \left(\frac{\pi a_V}{r_R A^{1/3}} \right)^2 \right) \quad (9)$$

for each nuclei. For example, even though the $\bar{n}$C experimental annihilation cross section at $p_{\text{lab}} > 500$ MeV/c is not readily available, according to Pomeranchuk's equality at the high-energy limit [55], both the $\bar{n}$C and $\bar{p}$C annihilation cross sections should be identical. Therefore, it is reasonable to make use of the experimental data to determine the value of $\bar{p}$C annihilation cross section at 900 MeV/c and use this value to determine the r_R, which turns out to be 1.653 fm. Concerning how one guesses the value of the diffuseness parameter a_V, its initial estimate is deduced from the clues given by Friedman [31], in which the a_V for antineutron may be about a factor of 2–3 times of that for the neutron. To search for the optimal value of a_V, several iterative calculations for annihilation cross section have to be performed at a fixed momentum of 900 MeV/c for both $\bar{n}$C and $\bar{p}$C until both their annihilation cross sections closely satisfy Pomeranchuk's equality. Once the r_R and a_V values are determined, Eq. (9) gives the corresponding value of r_V. The same procedure is also applied to the case of iron nuclei.

With respect to the Al, Cu, Sn, and Pb nuclei (e.g., see Fig. 5 in Ref. [9]), despite the fact that there are $\bar{p}$ experimental data are available at around 1 GeV/c, they were not measured at a common momentum point. As a result, we are afraid that they can complicate the consistency of our estimations for the r_R and hence r_V values for each element. To be safe, we choose to use the experimental $\bar{n}A$ annihilation cross section values at 375 MeV/c and extrapolate them to 400 MeV/c. Note that

TABLE II. The estimated annihilation cross sections at 400 and 900 MeV/c, and their corresponding values of r_R.

Pair	p_{lab} (MeV/c)	$\sigma = \pi (r_R A^{1/3})^2$ (fm^2)	r_R (fm)
$\overline{p}$C	900	45.0	1.653
$\overline{n}$Al	400	100.0	1.881
$\overline{p}$Fe	900	100.0	1.475
$\overline{n}$Cu	400	180.0	1.893
$\overline{n}$Ag	400	240.0	1.840
$\overline{n}$Sn	400	265.0	1.868
$\overline{n}$Pb	400	400.0	1.911

the same iterative a_V-search procedure is also considered for these elements. Table II presents the annihilation cross sections at 400 and 900 MeV/c, and their corresponding values of r_R. The subsequent antineutron radial and diffuseness parameters for the POMP as a function of mass numbers are given in Table III. Figure 6(a) illustrates the variation of the strength of V_o as a function of mass number and antineutron momentum. In general, their behaviors bear similarity with the momentum functional form of $\sigma_{ann}^{\overline{n}A}$.

In order to obtain the nA reaction cross section, we adopted the optical model potential by Koning and Delaroche [60]. To avoid later confusion, we shall use the phenomenological optical model potential (POMP) to denote the antinucleon-nucleus interactions $U(r)$ of Eq. (7). On the other hand, we shall use the Koning-Delaroche optical model potential (KD-OMP) to denote the nA optical potential described in Ref. [60].

These optical model potentials are then employed in the Schrödinger equation, and the standard distorted wave method provided in the ECIS97 computer program [63] is used to solve the Schrödinger equation to obtain the reaction cross section. For each individual nucleus, we use a fixed value for V_o evaluated at $p_{lab} = 200$ MeV/c for $p_{lab} \geqslant 200$ MeV/c, as V_o becomes almost constant in the high-energy limit. Furthermore, we also check the sensitivity of the cross section at $p_{lab} = 200$ MeV/c with respect to the small variation ($\sim$5%) of V_o and make sure that the change in the cross section is not more than $\sim$5%.

TABLE III. Optical model potential parameters for $\overline{n}A$ and nA interactions. The neutron optical model potential parameters are from Ref. [60]. The geometry parameters r_x and diffusiveness parameters a_x are in fm. It is assumed that $r_W = r_V$, $a_W = a_V$, $a_{V_D} = a_{W_D}$, and $V_D = 0$.

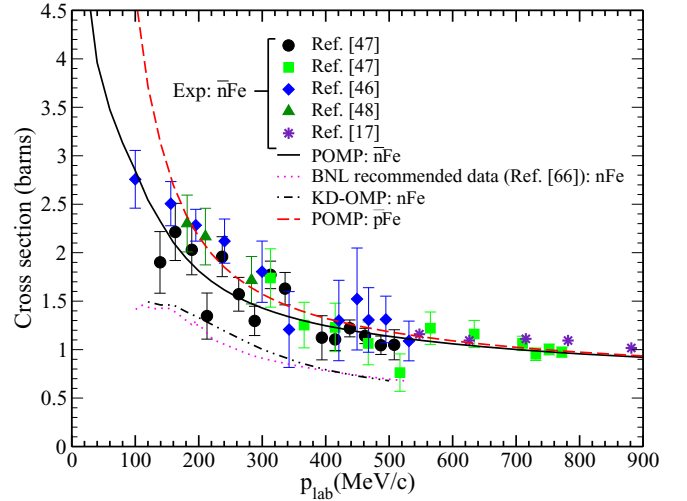| Nucleus		^{12}C	^{27}Al	^{56}Fe	^{64}Cu	^{108}Ag	^{119}Sn	^{206}Pb
$\overline{n}$	r_V	1.234	1.577	1.307	1.649	1.663	1.681	1.785
	r_{W_D}	1.260	1.260	1.260	1.260	1.260	1.260	1.260
	a_V	1.050	1.250	1.050	1.500	1.500	1.600	1.600
	a_{W_D}	0.590	0.590	0.590	0.590	0.590	0.590	0.590
n	r_V	1.127	1.162	1.186	1.203	1.219	1.221	1.235
	r_{W_D}	1.306	1.290	1.282	1.279	1.267	1.264	1.249
	a_V	0.676	0.665	0.663	0.668	0.662	0.660	0.647
	a_{W_D}	0.543	0.538	0.532	0.534	0.527	0.525	0.510

FIG. 2. Comparison of $\overline{n}$Fe, $\overline{p}$Fe annihilation cross sections and the nFe nonelastic reaction cross section as a function of the projectile momentum in the laboratory frame. The symbols are experimental data of $\overline{n}$Fe annihilation. The dash-dot-dotted line refers to the nFe reaction cross section obtained using the KD-OMP; the dotted line is the nFe reaction nonelastic data from Brookhaven National Laboratory's National Nuclear Data Center [66].

III. RESULTS AND DISCUSSION

In this section, we first evaluate our $\overline{n}A$ annihilation cross section results by comparing with the available experimental data. Second, we discuss the differences between the $\overline{n}A$ annihilation and nA reaction cross sections, and compare their corresponding optical model potential parameters. Third, we consider the $\overline{p}A$ annihilation. Lastly, we analyze the power laws of the $\overline{p}$ and $\overline{n}$ annihilation cross sections.

A. $\overline{n}A$ annihilation cross sections

In our previous study [23], we examined the $\overline{n}p$ annihilation cross section as a function of the antineutron momentum by considering the transmission through a nuclear potential. Although the annihilation cross section data for $\overline{n}p$ still remain rather sparse to date in comparison to $\overline{p}p$ and contain significant degrees of uncertainty, a good agreement is achieved between our analytical results and experimental data from the OBELIX Collaboration [1] and from Brookhaven National Laboratory [2]. Similarly, a good way to verify and validate the present optical model potential model in describing the mass A and momentum dependencies of $\overline{n}$ annihilation (and of n reactions) is to benchmark against the available experimental data.

Figure 1 shows a comparison of $\overline{n}$C annihilation cross sections against several sets of data. From a quantitative perspective, the predicted cross sections appear to obey the momentum dependence behavior suggested by the experiment in the low-momenta region. As p_{lab} proceeds to increase beyond 500 MeV/c, the theoretical and experimental cross sections continue to remain in agreement, indicating that the cross section decreases as the momentum increases.
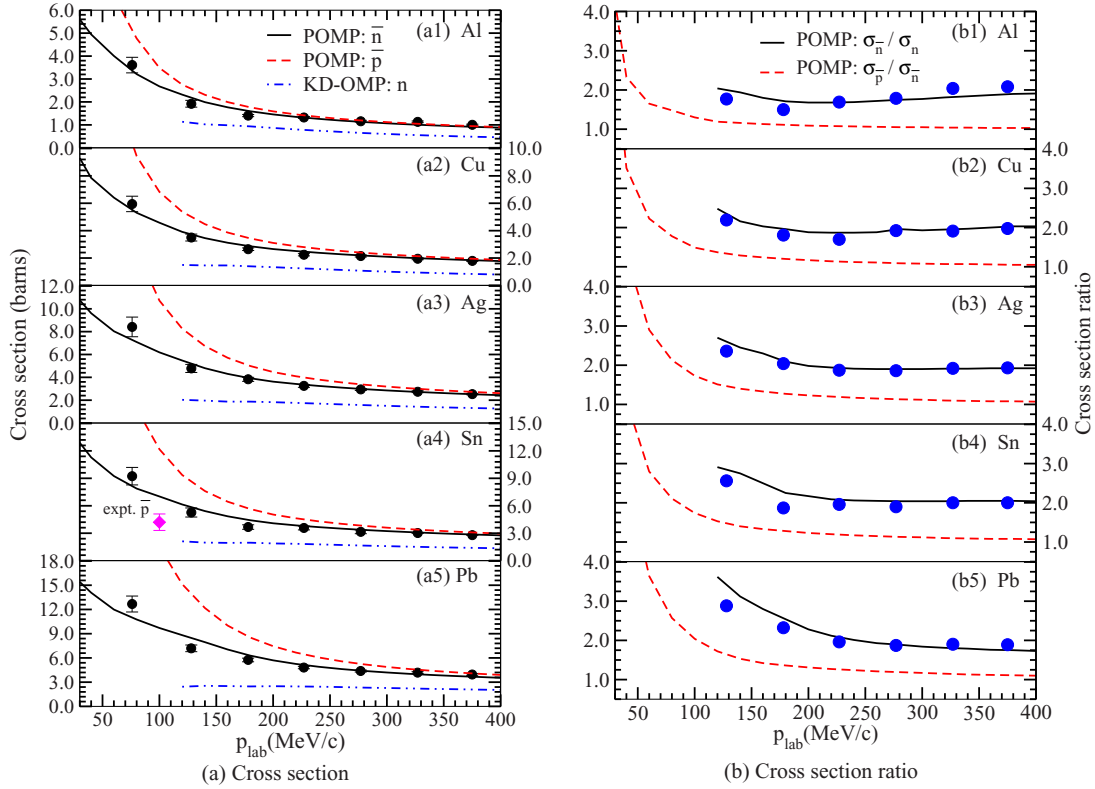
FIG. 3. (a) Cross sections for $\overline{n}A$, $\overline{p}A$, and nA as a function of the projectile momentum in the laboratory frame. The solid line is for $\overline{n}A$, the dashed line is for $\overline{p}A$, and the dash-dot-dotted line is for nA. The circles are experimental data from Astrua *et al.* [8]. The diamond is from Bianconi *et al.* [9]. (b) Cross section ratios. The solid line represents the theoretical $\sigma_{\mathrm{ann}}^{\overline{n}A}/\sigma_{\mathrm{rec}}^{nA}$, the dashed line represents the theoretical $\sigma_{\mathrm{ann}}^{\overline{p}A}/\sigma_{\mathrm{ann}}^{\overline{n}A}$, and the solid circle represents the ratio of the experimental $\sigma_{\mathrm{ann}}^{\overline{n}A}$ to the theoretical $\sigma_{\mathrm{rec}}^{nA}$.

In Fig. 2, we examine the $\overline{n}$Fe annihilation cross sections along with several data sets. Similarly, the calculated $\overline{n}$Fe annihilation cross sections also appear to be in good agreement with the experimental data, which indicate much larger cross sections (in comparison to the case of $\overline{n}$C annihilation) below p_{lab} of 400 MeV/c, and the annihilation cross section becomes progressively smaller as one goes up in p_{lab}.

Figure 3(a) shows that the predicted $\overline{n}A$ annihilation cross sections for the Al, Cu, Ag, Sn, and Pb nuclei rise considerably as the projectile momentum continues to decrease. These theoretical cross sections also describe the experimental data [8] relatively well in the momenta region where the data are available for comparison, except at p_{lab} of 76 MeV/c where the calculations underestimated the experiment by about 15–20% for Ag, Sn, and Pb targets. In regard to the finding of Ref. [32] where $\overline{n}$ annihilation cross sections shift to lower and lower momentum as nuclear size increases, inspecting the change of $\sigma_{\mathrm{ann}}^{\overline{n}A}$ cross sections as a function the nuclear mass number A displayed in Fig. 3(a), we do not notice any sign of reduction of $\overline{n}A$ annihilation cross sections or shifts of such kind.

B. nA reaction cross sections

The energy dependence of nA reaction cross sections have been relatively well studied for many elements across the periodic table over the years. Therefore, it is meaningful to compare the $\overline{n}A$ annihilation cross section against the nA

reaction cross section as a function of incoming projectile momentum. But before we do that, it is worthwhile to examine the quality of the present neutron reaction cross sections based on the KD-OMP. Displayed in Fig. 4 is a comparison between the present results and the BNL recommended nonelastic reaction cross section data for C, Al, Fe, Cu, Ag, and Pb nuclei [66]. It is shown that the overall agreement between the calculated cross sections and recommended data is reasonably good. Note that we intentionally left out the Sn results in the plot because, to our best knowledge, we could not find the available BNL data to make a comparison.

Since both the $\overline{n}A$ and nA interactions are free from initial-state Coulomb interactions, it is valuable to compare the momentum dependence of the cross sections of these two interactions. One can clearly see, from Figs. 1, 2, and 3(a), that the $\overline{n}$ annihilation cross sections of all targets are significantly larger than that of the n reaction. To better appreciate the differences in the cross sections between the $\overline{n}$ and n projectiles, we plot the $\sigma_{\mathrm{ann}}^{\overline{n}A}/\sigma_{\mathrm{rec}}^{nA}$ ratios as a function of the projectile momentum for carbon and iron nuclei in Fig. 5(a). In general, the curves for carbon and iron nuclei depict a similar behavior. In the same plot, we also include the ratio of experimental $\sigma_{\mathrm{ann}}^{\overline{n}C}$ to the theoretical $\sigma_{\mathrm{rec}}^{nC}$, which we shall denote as the experimental ratio. It is interesting to see the shape of the curve of experimental ratios also resembles the behavior of the theory even though the agreement between the theoretical predicted and the experimental ratios is not
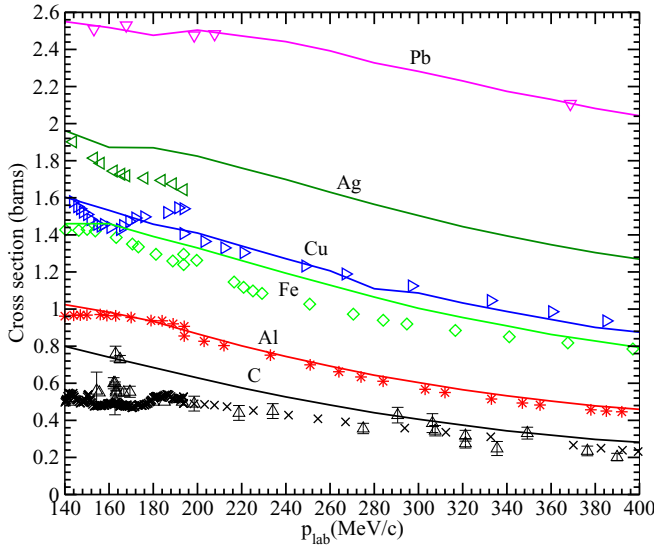
FIG. 4. The nA nonelastic reaction cross section as a function of the projectile momentum in the laboratory frame. The solid line refers to the present results obtained using the KD-OMP. The symbols are the data recommended by the Brookhaven National Laboratory's National Nuclear Data Center [66].

that satisfactory. The disagreement may be attributed to the calculation not taking into account the effects of static and dynamical deformation of the carbon nuclei.

Examining Fig. 5(a) more closely, one finds that the theoretical $\sigma_{ann}^{\bar{n}C}/\sigma_{rec}^{nC}$ ratio is about 1.5 at $p_{lab} \simeq 160$ MeV/c whereas the experimentally suggested value is about 1.3 and at a slightly higher p_{lab} of 165 MeV/c. Moving to higher
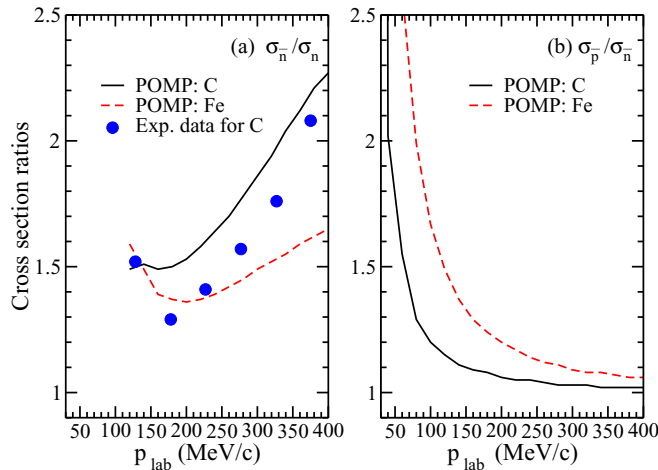
FIG. 5. Cross section ratios as a function of the projectile momentum in the laboratory frame. (a) The ratios of $\sigma_{\bar{n}}/\sigma_n$. The solid line represents the theoretical $\sigma_{ann}^{\bar{n}C}/\sigma_{rec}^{nC}$, the dashed line represents the theoretical $\sigma_{ann}^{\bar{n}Fe}/\sigma_{rec}^{nFe}$, and the solid circle represents the ratio of experimental $\sigma_{ann}^{\bar{n}C}$ to the theoretical σ_{rec}^{nC}. Note that there are no experimental $\sigma_{ann}^{\bar{n}Fe}$ available at the common momentum points of carbon. (b) The ratios of $\sigma_{\bar{p}}/\sigma_{\bar{n}}$. The solid line represents the theoretical $\sigma_{ann}^{\bar{p}C}/\sigma_{ann}^{\bar{n}C}$ and the dashed line represents the theoretical $\sigma_{ann}^{\bar{p}Fe}/\sigma_{ann}^{\bar{n}Fe}$.

$p_{lab} \simeq 400$ MeV/c, this ratio is about 2.3. It should be noted that in this low-energy region we have assumed that most of the nA nonelastic reactions are due to the absorption process. We also restrict our analysis to the lowest momentum of 100 MeV/c to avoid any complications due to contributions from the low-energy resonances.

Again, as illustrated in Fig. 5(a), the $\sigma_{ann}^{\bar{n}Fe}/\sigma_{rec}^{nFe}$ ratio also turned out to be about 1.4 to 1.6 between p_{lab} values of 120 and 400 MeV/c. For the rest of the targets shown in Fig. 3(b), one finds that the $\sigma_{ann}^{\bar{n}A}/\sigma_{rec}^{nA}$ ratios vary between the order of 1.5 and 3.8 in the region where comparisons are possible, and also depend on both the momentum and the A values. Notice that their momentum dependency of cross section ratios resembles their cross section behaviors, which are also quite different from those of the iron and carbon nuclei seen earlier in Fig. 5(a). Comparing to the case of carbon nuclei, Fig. 3(b) indicates a much better agreement between the predicted and the experimental $\sigma_{ann}^{\bar{n}A}/\sigma_{rec}^{nA}$ ratios for all targets. The better agreement is understandable since the theoretical and experimental σ_{rec}^{nA} are also in a much closer agreement (e.g., see Fig. 4).

Now we consider the optical potential parameters for both $\bar{n}A$ and nA interactions. The values of the initial (or starting) potential depth V'_o for all the target elements are given in Table I. The V'_o value, in general, increases from 52 to 110 MeV as the A value goes from 12 to 206. But with KD-OMP [60] calculations, this trend is reversed for the case of the nA reaction.

The corresponding real parts of the central potentials V_o for $\bar{n}A$ and nA interactions, as a function of momentum, are shown in Figs. 6(a) an 6(b), respectively. Although the depth of V_o based on POMP for every nuclei decreases with increasing momentum according to Eq. (7), as shown in Fig. 6(a), the antineutron's potential curves do not display any form of systematic order as a function of mass number A. At larger momentum (i.e., $p_{lab} > 100$ MeV/c), the potentials gradually become less sensitive to the increment of the projectile momentum. In contrast, in Fig. 6(b), the neutron's V_o obtained from KD-OMP [60] for each nucleus does show a systematic decrease as the nuclear size increases and an almost linear decrease as a function of momentum, especially for $p_{lab} > 200$ MeV/c.

The imaginary terms W_o and W_{o_D}, the volume and surface absorption POMP components, are also quite different from the KD-OMP prescribed values. First of all, they do not depend on projectile momentum. Second, as shown in Table II, even though our W_o for $\bar{n}A$ varies from 12.0 to 2.8 MeV with respect to carbon and to lead nuclei, there is no systematic change in W_o as the nuclear size increases. In comparison to the case of nA, Fig. 7(a) shows that the KD-OMP determined W_o decreases as A value increases, but increases as p_{lab} increases. Third, the antineutron's surface absorption W_{o_D} for $\bar{n}A$ is chosen to be a constant of 5.98 MeV for all targets. However, the neutron's surface absorption values W_{oD} do depend on momentum, and their functional forms are diaplayed in Fig. 7(b). It should be noted that for neutrons, at low incident energy, the absorption is dominated by the surface component W_{o_D}. Beyond about 250 MeV/c, the volume term W_o can no longer be ignored, and at higher energies the absorption can be completely dominated by W_o.
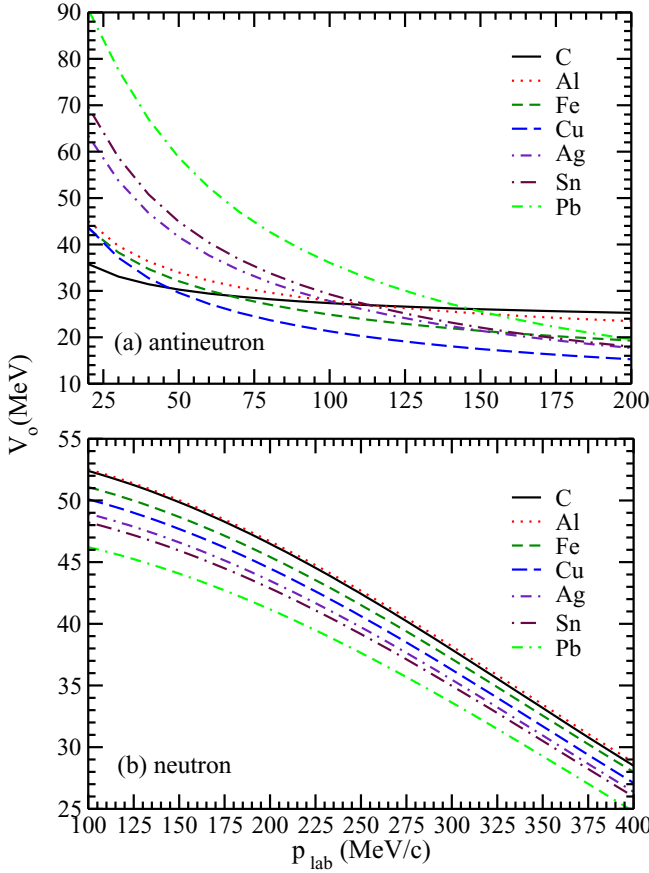
FIG. 6. The variation of V_o as a function of projectile momentum and atomic mass.

FIG. 7. Neutron optical model potential well depth, $W_{(o,o_D)}$, as a function of projectile momentum.

We compare the geometrical parameters r_x and diffusiveness parameters a_x for $\bar{n}A$ and nA interactions in Table III. Similar to nA interactions, with the case of iron nuclei as an exception, we have in the case of $\bar{n}A$ that the radii $r_W = r_V$ and they increase as A increases. But the present r_V values for the antineutron are significantly larger than those for the neutron. For example, the r_V of 1.785 fm for $\bar{n}$Pb annihilation is about 45% larger than the r_V of 1.235 fm for the nPb reaction. Also, in the $\bar{n}A$ case, even though the r_{W_D} values for $\bar{n}A$ and nA are not that different, we have a constant value of $r_{W_D} = 1.26$ fm for every nuclei, whereas the r_{W_D} associated with the nA reaction decreases from the C target with $r_{W_D} = 1.306$ fm to Pb with $r_{W_D} = 1.249$ fm. A similar pattern is also found with the $\bar{n}A$ diffusiveness parameters $a_W = a_V$ and a_{W_D}. The diffusiveness parameters a_V for $\bar{n}A$ also happen to be at least a factor of 2–3 larger than those for the nA interactions. Nevertheless, this set of POMP parameters enables us to obtain theoretical cross sections that complement the experimental annihilation cross sections across a wide momentum range.

C. $\bar{p}A$ annihilation cross sections

As an adjunct to predicting the $\bar{n}A$ annihilation and nA reaction cross sections, we further predict the $\bar{p}A$ annihilation cross section. We base our prediction on the simplest assumption that both $\bar{p}A$ and $\bar{n}A$ interactions have the same nuclear optical
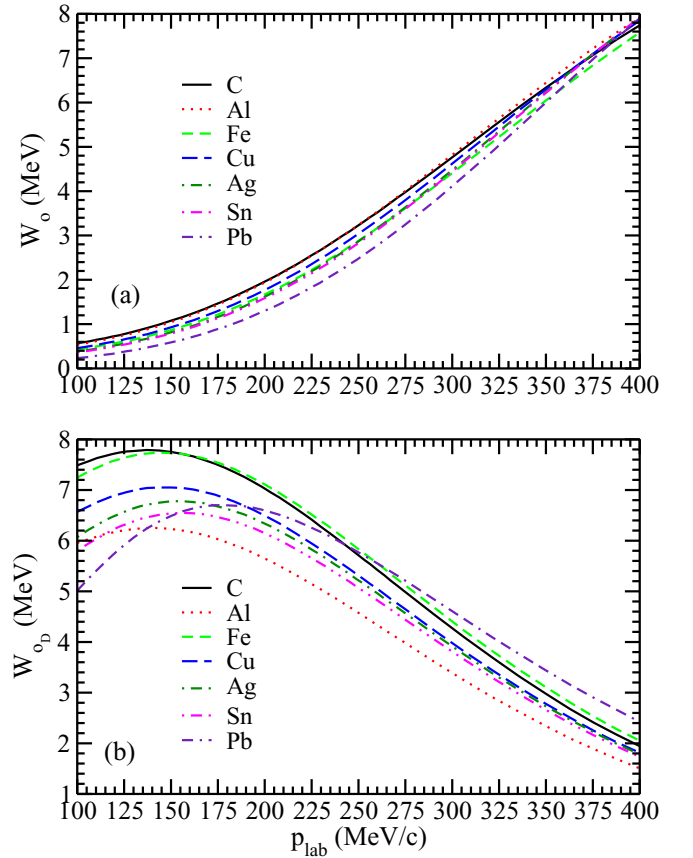
model potential but differ only in the long-range Coulomb interaction. The goal here is to examine the dependence of the annihilation cross sections on the projectile charge and to provide a benchmark for comparison, against which the $\bar{n}A$ and $\bar{p}A$ interaction potentials may differ.

In comparison to the neutral $\bar{n}$ projectile, according to the annihilation cross sections depicted in Figs. 1, 2 and 3(a), it is within our expectation that the charged $\bar{p}$ projectile shows relatively larger annihilation cross section. As a matter of fact, because of the additional effects from Coulomb focusing, the $\bar{p}$ annihilation cross sections for all the nuclei feature a steeper rise than that of the $\bar{n}A$ interaction as the projectile momentum goes down. As the projectile momentum continues to increase, the effects from Coulomb focusing also gradually diminish. As a result, the annihilation cross sections for both $\bar{n}$ and $\bar{p}$ merge at $p_{\text{lab}} \sim 500$ MeV/c, and eventually reach Pomaranchuk's equality, in which their cross section ratio becomes unity at ~ 1.0 GeV/c. These plots also evidently indicate that the $\bar{p}A$ annihilation cross sections are sensitive to the target mass number A.

To better understand the differences in annihilation cross sections due to $\bar{p}$ and $\bar{n}$ projectiles, we examine the $\sigma_{\text{ann}}^{\bar{p}A}/\sigma_{\text{ann}}^{\bar{n}A}$ ratios as a function of momentum for carbon and iron nuclei in Fig. 5(b). The plots show that their behavior is similar to the momentum dependence of their annihilation cross sections, and their slopes are remarkably steep in the region where the
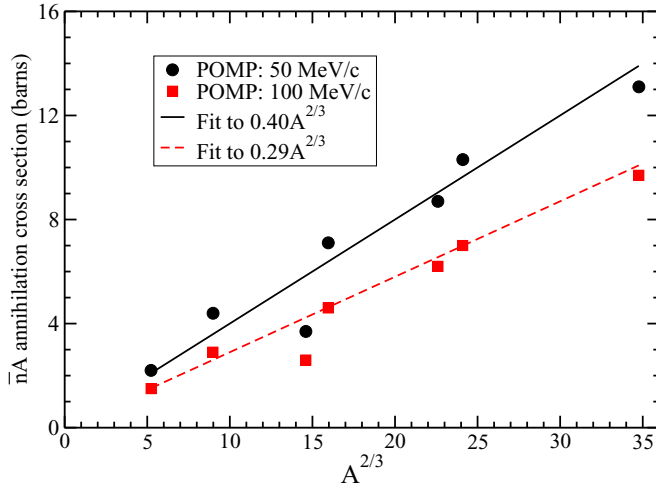
FIG. 8. Antineutron annihilation cross sections as a function of atomic mass number $A^{2/3}$ at $p_{\rm lab} = 50$ and 100 MeV/c. The scattered points are results from POMP calculations. The solid and dashed lines are results from the fitting to the expression $\sigma_{\rm ann}^{\bar{n}A} = \sigma_o^{\bar{n}A} A^{2/3}$.

FIG. 9. The exponent α expressing the dependence of the $\sigma_{\rm ann}^{\bar{n}A}$ and $\sigma_{\rm ann}^{\bar{p}A}$ on $p_{\rm lab}$ as $\sigma_{\rm ann}^{\bar{n}A} \propto 1/p_{\rm lab}^{\alpha}$, as a function of the target mass number A. The scattered points are results from the present POMP calculations. The dashed line marks $\alpha = 0.530$ (an average over all the targets) for the $\bar{n}$ projectile whereas the dotted line marks $\alpha = 1.494$ (an average over all the targets) for the $\bar{p}$ projectile.

momentum goes to zero. Comparing the magnitude of the iron ratio curve to that of carbon, one clearly sees a stronger Coulomb focusing effects for the heavier nucleus and this long-range effect weakens in the limit of large momentum. In addition to that, Fig. 5(b) also reveals a contrasting energy dependent in the behavior of $\sigma_{\rm ann}^{\bar{p}A}/\sigma_{\rm ann}^{\bar{n}A}$ ratios in comparison to those of $\sigma_{\rm ann}^{\bar{n}A}/\sigma_{\rm rec}^{nA}$ ratios shown in Fig. 5(a).

Figure 3(b) displays a collection of the behaviors of $\sigma_{\rm ann}^{\bar{p}A}/\sigma_{\rm ann}^{\bar{n}A}$ ratios for all target nuclei as a function of momentum. The featured behavior is consistent with $\sigma_{\rm ann}^{\bar{n}A}/\sigma_{\rm rec}^{nA}$ where comparisons are possible, expected that the $\sigma_{\rm ann}^{\bar{p}A}/\sigma_{\rm ann}^{\bar{n}A}$ ratios are smaller by roughly a factor of 2. Again, all the $\sigma_{\rm ann}^{\bar{p}A}/\sigma_{\rm ann}^{\bar{n}A}$ ratios show strong momentum dependence at low momenta.

Recently, the ASACUSA Collaboration took a new measurement of the $\bar{p}$C annihilation cross section at a low energy of 5.3 MeV or $p_{\rm lab} = 100$ MeV/c [20]. Their cross section value of 1.73 ± 0.25 barns is also plotted in Fig. 1. The datum clearly touches our prediction. In addition to that, we have also plotted the one and only experimental datum for $\bar{p}$Sn at 100 MeV/c in Fig. 3(a4). The down side of this case is that there are no other comparable experimental measurements for $\bar{p}$ and $\bar{n}$ as in the case of protons. Therefore, at this point, we will not surmise the energy dependence of the $\bar{p}$Sn cross section.

D. The power laws and annihilation cross sections

Since it is of interest to find out whether $\sigma_{\rm ann}^{\bar{n}A} \propto A^{2/3}$ at low energies, we plotted $\sigma_{\rm ann}^{\bar{n}A}$ at $p_{\rm lab} = 50$ and 100 MeV/c against the corresponding mass number of $A^{2/3}$ in Fig. 8. The scattered points are the POMP predicted results. They are fitted with an expression of $\sigma_{\rm ann}^{\bar{n}A} = \sigma_o^{\bar{n}A} A^{2/3}$. The fitting is rather good. It indeed indicates that $\sigma_{\rm ann}^{\bar{n}A}$ has a linear dependence on $A^{2/3}$ at low energies. Apart from these, Fig. 8 additionally reveals that the $\bar{n}$Fe annihilation cross sections appear to peculiarly deviate from this linear dependence. Perhaps future experiments can
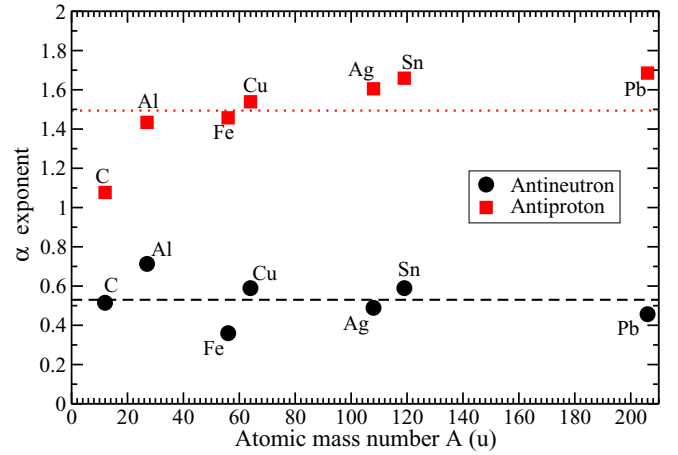
reinvestigate this anomaly in the low-momentum region where $p_{\rm lab}$ is less than 100 MeV/c.

It is also informative to examine the inverse power law of $\bar{n}A$ annihilation. In the limit of low energy, parametrizing the theoretical annihilation cross section in an inverse power law form, $\sigma_{\rm ann}^{\bar{n}A} \propto 1/p_{\rm lab}^{\alpha}$, in the range between 40 and 100 MeV/c, the α exponential value can be easily determined by setting $\alpha = \partial \ln(\sigma_{\rm ann})/\partial \ln(p_{\rm lab})$. Figure 9 gives the variation of α exponential values as a function of mass number A. Taking an average over all the nuclear targets yields a value of $\alpha = 0.530$. This consequently suggests that the $\sigma_{\rm ann}^{\bar{n}A}$ may be proportional to $1/p_{\rm lab}^{1/2}$ for targets with $A \geqslant 6$. This finding appears to be far from what we learned in our previous work [23]. There we found in the case of $\bar{n}p$ the exponential value $\alpha = 1.08$ in the momentum range between 30 and 95 MeV/c. This exponential value is very close to the expected $\alpha = 1.0$ value, a clear indication of the $1/p_{\rm lab}$ behavior. However, in our previous study [23], the nuclear potential was assumed to be a constant there. Here, in contrast, the nuclear optical potential depends on the projectile momentum, causing the $\sigma_{\bar{n}A}$ to deviate from the $1/p_{\rm lab}$ law.

At the low-energy limit, we can see that the cross section slope for the $\bar{p}A$ interaction is much steeper than the one of $\bar{n}A$. Therefore, it is also meaningful to check the inverse power law form, $\sigma_{\rm ann}^{\bar{p}A} \propto 1/p_{\rm lab}^{\alpha}$, of $\bar{p}A$ annihilation. Similar to what we discussed earlier with respect to $\bar{n}A$ annihilation in Fig. 9, parametrizing the theoretical annihilation cross section in a power law form in the range between 40 and 100 MeV/c allows one to obtain the α exponential value. In our previous investigation on $\bar{p}p$ interaction [23], we found that $\alpha = 1.544$ in the momentum range between 30 and 50 MeV/c. Displayed in Fig. 9 is the variation of α as a function of mass A. Similarly, averaging these values over the seven nuclear targets yields a value of $\alpha = 1.494$. As opposed to the case of $\bar{n}A$, this value is close to what we found previously in the case of $\bar{p}p$

annihilation. This also means the Coulomb effect is dominant at the low-energy limit and cannot be neglected. The extracted $\alpha = 1.494$ is not quite equal to $\alpha = 2.0$ as expected at the very-low-energy limit [64,65]. This means that the approach to the lowest energy limit of $\alpha = 2$ will occur at much lower energies than the range of low energies considered here.

IV. SUMMARY AND CONCLUSIONS

The purpose of this contribution is twofold. The first one is to revisit and rectify our previous annihilation cross section results for $\bar{n}A$ in [23]. The second one is to pursue a phenomenological analysis of $\bar{n}$ annihilation cross section as a function of projectile momentum p_{lab} and mass number A.

Previously, we used the extended Glauber theory [23] to examine the experimental annihilation cross section data for $\bar{n}$ on C, Al, Fe, Cu, Ag, Sn, and Pb in the momentum range below 500 MeV/c. But an inadvertent error arose through the Coulomb trajectory modification, causing the results to agree with the experimental data. After amending the theory, the re-evaluated results turned out to be in disagreement with the experimental data.

The Glauber theory is well known to be valid for high-energy collisions in which the extend individual nucleon can be treated as an isolated scatterer. For low-energy collisions, such a description may not be as appropriate and the traditional optical model analysis may be more suitable. For this reason we adopt the optical model potential to analyze the momentum dependence of $\bar{n}A$ annihilation cross section.

The use of a microscopic optical model potential method was previously attempted by Friedman [31,32] to investigate the momentum dependence of $\bar{n}A$ annihilation cross sections. The investigation found that the annihilation cross section of $\bar{n}$ on nuclei cannot be described by a microscopic optical potential that fits well the available data on the $\bar{p}$ interactions with nuclei. Nevertheless, inspired by the works of Friedman and Koning and Delaroche [60], we explored a new form of momentum-dependent optical model potential to describe the $\bar{n}A$ interaction. Even though it is phenomenological and local, the presented optical model potential of Eq. (7) is quite different from that of Koning and Delaroche and that of Friedman. It is simple, as well as comprehensive enough to treat very-low-momentum $\bar{n}A$ and $\bar{p}A$ annihilations. We employed the momentum-dependent optical model potential in the Schrödinger equation, and the equation is solved using

the standard distorted wave method provided in the ECIS97 computer program [63] to evaluate the annihilation cross sections for $\bar{n}A$ and $\bar{p}A$. Similarly, we have also applied the Koning-Delaroche's momentum-dependent optical model potential to examine the nA nonelastic reaction cross sections on on C, Al, Fe, Cu, Ag, Sn, and Pb. We showed that the calculated cross sections are in reasonable agreement with the recommended data from Brookhaven National Laboratory's database.

Although, in this study, we found that the present $\bar{n}A$ annihilation cross sections fit the experimental data rather well, this does not mean that we have fundamentally understood the neutral $\bar{n}A$ annihilation mechanism. In fact, the opposite is true. For a start, even though both the $\bar{n}A$ and nA interactions are Coulomb free, why does the $\sigma_{\mathrm{ann}}^{\bar{n}A}/\sigma_{\mathrm{rec}}^{nA}$ cross section ratio appears to be so large (almost by a factor of 2)? From a simple geometrical argument, in comparison to the incoming neutron n, why does the antineutron $\bar{n}$ seems to have a larger "effective area" for the target nuclei to react? Further theoretical and experimental efforts are necessary to address these fundamental questions.

In the low-energy range considered here, we have demonstrated and verified that $\sigma_{\mathrm{ann}}^{\bar{n}A}$ is indeed approximately proportional to $A^{2/3}$. We have illustrated that for neutral or Coulomb-free $\bar{n}A$ interactions the annihilation $\sigma_{\mathrm{ann}}^{\bar{n}A} \propto 1/p_{\mathrm{lab}}^{\alpha}$. In addition, we have also shown that the α value for charged $\bar{p}A$ interactions is significantly larger than the α value for neutral $\bar{n}A$ interactions. We presume that this is likely due to the additional Coulomb effects on top of nuclear interactions for charged $\bar{p}A$ interactions. In conclusion, we have calculated the $\bar{n}A$ annihilation cross section based on the simplest assumption that both $\bar{n}A$ and $\bar{p}A$ interactions have the same nuclear optical potential but differ only in the long-range electrostatic interaction. Any deviation from such a simple model extrapolation in measurements will shed new and desirable information on the difference between $\bar{n}A$ and $\bar{p}A$ potentials.

[1] A. Bertin *et al.*, Nucl. Phys. B, Proc. Suppl. A **56**, 227 (1997).

[2] T. Armstrong, C. Chu, J. Clement, C. Elinon, M. Furic, K. Hartman, A. Hicks, E. Hungerford, T. Kishimoto, J. Kruk, R. Lewis, D. Lowenstein, W. Lochstet, B. Mayes, R. Moss, G. S. Mutchler, L. Pinsky, G. A. Smith, L. Tang, W. vonWitsch, and Y. Xue, Phys. Rev. D **36**, 659 (1987).

[3] W. Brückner *et al.*, Z. Physik A – Atomic Nuclei **335**, 217 (1990).

[4] A. Bertin *et al.* (OBELIX Collaboration), Phys. Lett. B **369**, 77 (1996).

[5] A. Benedettini *et al.*, Nucl. Phys. B, Proc. Suppl. A **56**, 58 (1997).

[6] A. Zenoni *et al.* (OBELIX Collaboration), Phys. Lett. B **461**, 405 (1999).

[7] F. Iazzi *et al.*, Phys. Lett. B **475**, 378 (2000).

[8] M. Astrua *et al.*, Nucl. Phys. A **697**, 209 (2002).

[9] A. Bianconi *et al.*, Phys. Lett. B **704**, 461 (2011).

[10] A. Bianconi *et al.*, Phys. Lett. B **481**, 194 (2000).

[11] A. Bianconi *et al.*, Phys. Lett. B **492**, 254 (2000).

[12] R. Bizzarri *et al.*, Nuovo Cimento A **22**, 225 (1974).

[13] A. Zenoni *et al.* (OBELIX Collaboration), Phys. Lett. B **461**, 413 (1999).

[14] F. Balestra *et al.*, Phys. Lett. B **230**, 36 (1989).

[15] F. Balestra *et al.*, Phys. Lett. B **149**, 69 (1984).

[16] F. Balestra *et al.*, Phys. Lett. B **165**, 265 (1985).

[17] K. Nakamura, J. Chiba, T. Fujii, H. Iwasaki, T. Kageyama, S. Kuribayashi, T. Sumiyoshi, T. Takeda, H. Ikeda, and Y. Takada, Phys. Rev. Lett. **52**, 731 (1984).

[18] F. Balestra *et al.*, Nucl. Phys. A **452**, 573 (1986).

[19] V. Ashford, M. E. Sainio, M. Sakitt, J. Skelly, R. Debbe, W. Fickinger, R. Marino, and D. K. Robinson, Phys. Rev. C **31**, 663 (1985).

[20] H. Aghai-Khozani *et al.*, Nucl. Phys. A **970**, 366 (2018).

[21] E. Klempt, C. Batty, and J.-M. Richard, Phys. Rep. **413**, 197 (2005).

[22] T. G. Lee and C. Y. Wong, Phys. Rev. C **89**, 054601 (2014).

[23] T. G. Lee and C. Y. Wong, Phys. Rev. C **93**, 014616 (2016).

[24] J. Mahalanabis *et al.*, Nucl. Phys. A **485**, 546 (1988).

[25] V. F. Kuzichev, Yu. B. Lepikhin, and V. A. Smirnitsky, Nucl. Phys. A **576**, 581 (1994).

[26] J. Carbonell and K. Protasov, Hyperfine Interact. **76**, 327 (1993).

[27] J. Carbonell, K. Protasov, and A. Zenoni, Phys. Lett. B **397**, 345 (1997).

[28] A. Bianconi, G. Bonomi, E. Lodi Rizzini, L. Venturelli, and A. Zenoni, Phys. Rev. C **62**, 014611 (2000).

[29] A. Gal, E. Friedman, and C. J. Batty, Phys. Lett. B **491**, 219 (2000).

[30] C. J. Batty, E. Friedman, and A. Gal, Nucl. Phys. A **689**, 721 (2001).

[31] E. Friedman, Nucl. Phys. A **925**, 141 (2014).

[32] E. Friedman, Hyperfine Interact. **234**, 77 (2015).

[33] V. V. Uzhinsky and A. S. Galoyan, arXiv:hep-ph/0212369.

[34] A. S. Galoyan and A. Polanski, arXiv:hep-ph/0304196.

[35] A. Galoyan, J. Ritman, A. Sokolov, and V. Uzhinsky, arXiv:0809.3804.

[36] A. S. Galoyan and V. V. Uzhinsky, Pis'ma Zh. Eksp. Teor. Fiz. **94**, 539 (2011) [JETP Lett. **94**, 499 (2011)].

[37] V. Uzhinsky, J. Apostolakis, A. Galoyan *et al.*, Phys. Lett. B **705**, 235 (2011).

[38] A. Galoyan and V. Uzhinsky, Hyperfine Interact. **215**, 69 (2013).

[39] A. Galoyan, V. Uzhinsky, and A. Ribon, Eur. Phys. J. Web Conf. **173**, 06005 (2018).

[40] B. P. Singh *et al.* (PANDA Collaboration), Eur. Phys. J. **A51**, 107 (2015).

[41] A. Galoyan, PoS **Baldin ISHEPP XXII**, 049 (2015).

[42] C. B. Dover, A. Gal, and J. M. Richard, Phys. Rev. D **27**, 1090 (1983); Phys. Rev. C **31**, 1423 (1985); Nucl. Instrum. Methods Phys. Res., Sect. A **284**, 13 (1989).

[43] L. A. Kondratyuk, JETP Lett. **64**, 495 (1996).

[44] E. Friedman and A. Gal, Phys. Rev. D **78**, 016002 (2008).

[45] D. G. Phillips *et al.*, Phys. Rep. **612**, 1 (2016)

[46] M. Agnello *et al.*, Eur. Phys. Lett. **7**, 13 (1988).

[47] C. Barbina *et al.*, Nucl. Phys. A **612**, 346 (1997).

[48] V. G. Ableev *et al.*, Nuovo Cimento A **107**, 943 (1994).

[49] R. J. Glauber, in *Lectures in Theoretical Physics, Vol. 1*, edited by W. E. Brittin and L. G. Dunham (Interscience, New York, 1959), p. 315.

[50] R. Glauber and G. Matthiae, Nucl. Phys. B **21**, 135 (1970).

[51] C. Y. Wong, Phys. Rev. D **30**, 961 (1984).

[52] C. Y. Wong, *Introduction to High-Energy Heavy-Ion Collisions* (World Scientific, Singapore, 1994).

[53] C. Y. Wong and T. G. Lee, Ann. Phys. (N.Y.) **326**, 2138 (2011).

[54] T. G. Lee, C. Y. Wong, and L. S. Wang, Chin. Phys. **17**, 2897 (2008).

[55] I. Pomeranchuk, JETP Lett. **30**, 423 (1956).

[56] FAIR - Facility for Antiproton and Ion Research, Green Paper, October 2009 (unpublished).

[57] W. Erni *et al.* (PANDA Collaboration), Eur. Phys. J. A **49**, 25 (2013).

[58] S. Maury (for the AD Team), The Antiproton Decelerator (AD), CERN Report No. CERN/PS 99-50 (HP), 1999 (unpublished).

[59] R. L. Varner, W. J. Thompson, T. L. McAbee, E. J. Ludwig, and T. B. Clegg, Phys. Rep. **201**, 57 (1991).

[60] A. J. Koning and J. P. Delaroche, Nucl. Phys. A **713**, 231 (2003).

[61] C. Y. Wong, A. K. Kerman, G. R. Satchler, and A. D. MacKellar, Phys. Rev. C **29**, 574 (1984).

[62] R. W. Hasse and W. D. Myers, *Geometrical Relationships of Macroscopic Nuclear Physics* (Springer-Verlag, Heidelberg, 1988).

[63] J. Raynal, Phys. Rev. C **23**, 2571 (1981); ECIS97, https://people.nscl.msu.edu/~brown/reaction-codes/home.html.

[64] E. P. Wigner, Phys. Rev. **73**, 1002 (1948).

[65] L. D. Landau and E. M. Lifshitz, *Quantum Mechanics* (Pergamon, Oxford, 1958).

[66] Brookhaven National Laboratory, National Nuclear Data Center (ENDF/B-VII.1), www.nndc.bnl.gov/sigma/index.jsp.